

Bias-dependent diffusion of H₂O molecules on an Al(111) surface

Satoshi Hagiwara^{1,*}, Chunping Hu², Satomichi Nishihara², and Minoru Otani^{1†}

¹*National Institute of Advanced Industrial Science and Technology (AIST),*

1-1-1, Umezono, Tsukuba,

Ibaraki 305-8568, Japan

²*AdvanceSoft Corporation, 4-3,*

Kanda Suruga-dai, Chiyoda-ku,

Tokyo 101-0062, Japan

(Dated: December 21, 2020)

Abstract

We investigate the process by which a water molecule diffuses on the surface of an Al(111) electrode under constant bias voltage by first-principles density functional theory. To understand the diffusion path of the water on the Al(111), we calculated the minimum energy path (MEP) determined by the nudged elastic band method in combination with constant electron chemical potential (constant- μ_e) methods. The simulation shows that the MEP of the water molecule, its adsorption site, and the activation barrier strongly depend on the applied bias voltage. This strong dependence of the water diffusion process on the bias voltage is in good agreement with the result of a previous scanning tunneling microscopy (STM) experiment. The agreement between the theoretical and experimental results implies that accurate treatment of bias voltage plays a significant role in understanding the interaction between the electric field and the surface of the material. Comparative studies of the diffusion process with the constant total number of electrons (constant- N_e) scheme show that the absence of strong interaction between the molecular dipole and the electric field leads to a different understanding of how water diffuses on a metal surface. The proposed constant- μ_e scheme is a realistic tool for the simulation of reactions under bias voltage not only using STM but also at the electrochemical interface.

*Electronic address: hagiwara.satoshi@aist.go.jp

†Electronic address: minoru.otani@aist.go.jp

I. INTRODUCTION

Fundamental studies on metal/water interfaces [1–4] have attracted much attention because understanding the process of water reactions at the interface plays a central role in a wide variety of applications such as catalysis[5] and fuel cells[6]. A recent experiment to investigate the electrochemical interface reportedly showed that the molecular structure of water strongly depends on the electrode potential [7]. Furthermore, an experiment in which scanning tunneling microscopy (STM) was used found that the applied bias voltage affected the activation barrier of water diffusion on a Pt surface [8]. To further understand the water diffusion processes and reactions, it is necessary to clarify the extent to which water adsorption and diffusion on the surface depends on the bias voltage.

First-principles density functional theory (DFT) [9, 10] is a powerful tool for investigating the molecular adsorption and diffusion at the surface. However, previous theoretical studies on water diffusion processes were mainly carried out without the bias-voltage [11–14]. Generally, the electrode potential is related to the electron chemical potential (μ_e) of the electrode, and the difference in μ_e between the two subjects defines the bias voltage. Thus, for a system to which a fixed bias voltage is applied, the value of μ_e of the electrode (or sample) surface must be constant. Therefore, to control the bias voltage in the simulation, we need to control μ_e [15–18] beyond the constraint of a fixed number of electrons (constant- N_e).

The quantum mechanical theory formulated under a grand-canonical ensemble is indispensable for a simulation with the fixed μ_e (constant- μ_e)[15–18]. Two flexible simulation methods within the constant- μ_e scheme have been proposed: The one is the fictitious charge particle (FCP) method developed by Bonnet et al. [19], and the other is the grand-canonical self-consistent field (GCSCF) method introduced by Sundararaman et al [20]. These grand-canonical methods based on DFT can be applied not only to the electrochemical interface [20–24] but also to a system subjected to a bias voltage such as in the STM experiment.

In this study, we carried out a first-principles study of the adsorption and diffusion processes a water molecule undergoes on the surface of Al(111) by varying the bias voltage using the FCP and GCSCF methods. To understand the dependence of water diffusion on the bias voltage, we computed the minimum energy path using the nudged elastic band (NEB) method [25–27] under constant bias voltage. Specifically, in the case of aluminum, it

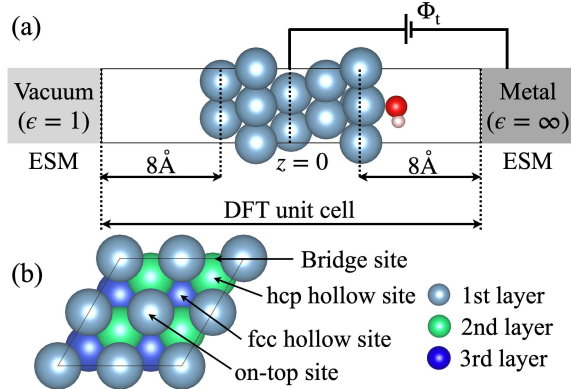


FIG. 1: (Color online). (a) Schematic view of the model under a bias voltage. The cyan, red, and pink spheres represent Al, O, and H atoms, respectively. The coordinate $z=0$ is defined as the center of the Al/H₂O system. Two ESM regions with dielectric constants $\epsilon=1$ and $\epsilon=\infty$, respectively, are attached to the left and right ends of the supercell to represent vacuum and the counter electrode (metal). (b) Adsorption sites on the Al(111) surface. The cyan, green, and blue spheres represent the first-, second-, and third-layer Al atoms, respectively, counting from the side of the counter electrode.

is essential to understand the fundamental processes at the metal/water interface [12, 28, 29]; thus, we used an aluminum electrode in our study.

The paper is organized as follows: Section II provides a brief description of the basic ideas of the constant- μ_e schemes, their computational procedures, and the computational details for the DFT and NEB calculations. In Sec. III, we discuss the results obtained by the NEB combined with the constant- μ_e scheme. Finally, the conclusions of our study are presented in Sec. IV.

II. METHODS AND COMPUTATIONAL DETAILS

Here, we describe the computational methods and details. First, we provide an overview of the constant- μ_e method under the boundary condition of the effective screening medium (ESM) technique [30]. The next subsection presents a discussion of the computational procedures of the FCP and GCSCF methods. Finally, we provide the computational details of the proposed method.

A. Constant- μ_e plus ESM method

First, we briefly describe the basics of the constant- μ_e scheme combined with the ESM method [30]. The ESM technique, which was developed by Otani and Sugino, is a powerful tool for studying various material surfaces under repeated slab approximation. Figure 1(a) shows a model of a constant- μ_e calculation combined with the ESM used in this study. Two ESM regions with dielectric constants $\epsilon = 1$ and $\epsilon = \infty$, respectively, are attached to the two ends of the supercell to represent the vacuum and the counter electrode (Metal). The electrostatic potential at the counter electrode was set to zero as the reference potential. Thus, the ESM enables us to always compare the energies measured from the same reference level.

To achieve the constant- μ_e condition, we use the FCP [19] and GCSCF methods [20]. Both of these methods can be used to compute the electronic structure and atomic geometry under the given target chemical potential μ_t . μ_t is imposed by a potentiostat at a potential Φ_t , as shown in Fig. 1(a), i.e. $\mu_t = -e\Phi_t$, where e is the charge of an electron. We can define the grand-potential Ω , instead of the total energy functional E_{tot} , as follows:

$$\Omega = E_{\text{tot}} - (N_e - N_e^0)\mu_t = E_{\text{tot}} - \Delta N_e \mu_t, \quad (1)$$

where ΔN_e is a fictitious charge particle, which is the difference between the total number of electrons in the system N_e and that in the neutral system N_e^0 . Then, we minimize the value of Ω for the atomic positions and ΔN_e , where ΔN_e is not a constant but a dynamic variable during the entire minimization procedure. Because both the FCP and GCSCF methods converge to the same physical state, we expect these two methods to yield the same results under the same computational conditions.

B. Computational procedure of constant- μ_e

Here, we discuss the practical minimization procedure for Ω in the FCP and GCSCF methods. Figure 2(a) and (b), respectively, show the flow charts for the calculations with FCP and GCSCF, where we show a series of flows for the DFT calculation with geometry optimization. The SCF and geometry optimization loops show the blue and green shaded areas, respectively. In the following two subsections, we discuss the FCP and GCSCF

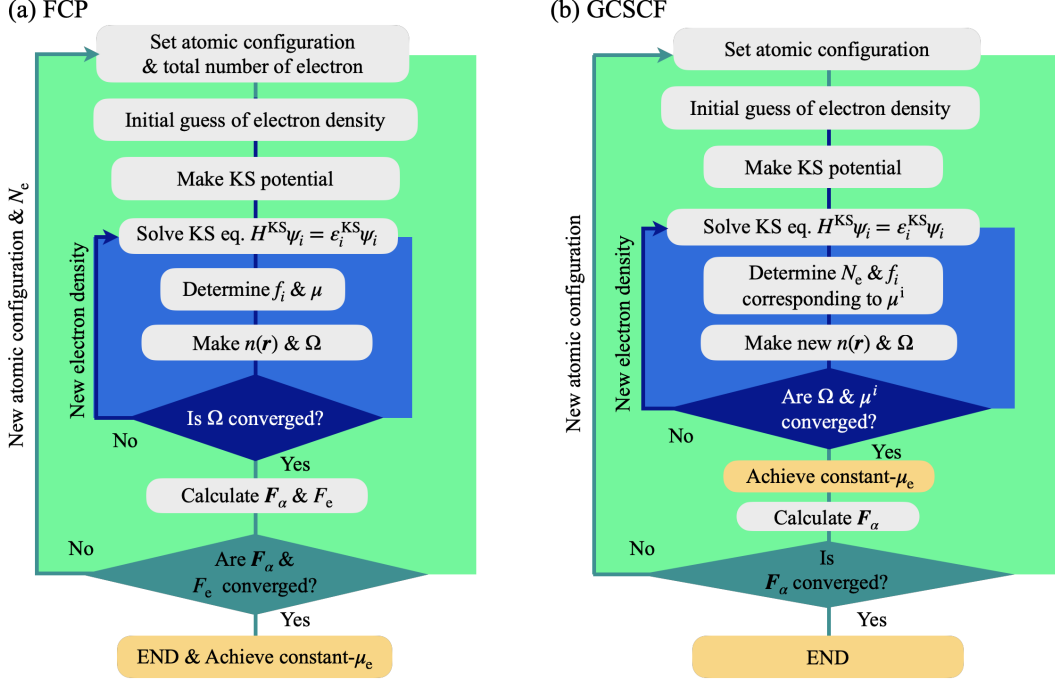


FIG. 2: (Color online). Calculation flows for (a) FCP and (b) GCSCF methods. The green and blue shaded areas, respectively, indicate the calculation loops for the geometry optimization and self-consistent field. Here, H^{KS} , ϵ_i^{KS} , and ψ_i denote the Kohn-Sham (KS) Hamiltonian, KS-eigenvalue, and KS-wavefunctions, respectively. The electron charge density is obtained by $n(\mathbf{r}) = \sum_i f_i |\psi_i(\mathbf{r})|^2$, where f_i is the occupation number for each state i . \mathbf{F}_α denotes the forces acting on each atom labeled by α .

methods using these flows.

1. FCP method

The FCP employs a grand-canonical ensemble by the system connecting to the fictitious potentiostat, as shown in Fig. 1(a), and minimizes Ω under the constraint of constant- μ_e in the loop in which the geometry is optimized, which is shown as the green shaded area. In the SCF loop shown as the blue shaded area, the Kohn-Sham equation is solved with the fixed number of electrons. Therefore, the system reaches constant- μ_e via simultaneously optimizing not only the atomic positions but also the total number of electrons N_e . To

optimize N_e , we define a fictitious force for N_e as

$$F_e = -\frac{\partial\Omega}{\partial N_e} = -\mu + \mu_t, \quad (2)$$

where, $\mu = \partial E_{\text{tot}}/\partial N_e$ implies the instantaneous μ_e , and yields the electrode potential as $\mu = -e\Phi$. To obtain N_e for μ_t , we minimize F_e using the quasi-Newton algorithm by using the Broyden-Fletcher-Goldfarb-Shanno minimization method [31–34]. This method is commonly used for geometry optimization in conjunction with DFT calculations. In the geometry optimization with the quasi-Newton algorithm, the following equation updates all degrees of freedom for the atomic positions at the k -th iteration (\mathbf{x}_k), until all forces acting on the atoms become zero, as follows:

$$\mathbf{x}_{k+1} = \mathbf{x}_k + \mathbf{h}_k \mathbf{f}_k. \quad (3)$$

Here, \mathbf{f}_k and \mathbf{h}_k denote the forces acting on the atoms and Hessian, respectively. In conventional geometry optimization, the motion of N atoms in three dimensions produces $3N$ degrees of freedom. In the FCP, both F_e and N_e are included in \mathbf{f}_k and \mathbf{x}_k , respectively. Thus, we explore the solution of eq. (3) within the space of the $3N + 1$ -th dimension. However, we cannot directly treat F_e and N_e on equal footing with \mathbf{f}_k and \mathbf{x}_k because the units of N_e and F_e are different from the atomic positions and forces. To address this, we introduce the effective charge position ($N'_e = \alpha N_e$), where α is a scaling factor unit in bohr/ e . F_e is also scaled by α as follows,

$$F'_e = (-\mu + \mu_t)/\alpha. \quad (4)$$

Here, the definition of α is $\alpha = L_{\text{max}}/V_{\text{max}}C_0$. L_{max} and V_{max} are the upper-bound of the change in the length and voltage at each step, respectively. C_0 is the capacitance determined by the formula of the parallel-plate capacitor:

$$C_0 = \frac{1}{4\pi} \frac{S}{L}. \quad (5)$$

Here, S denotes the surface area. Although the original definition of L is the distance between the parallel plates of the capacitor, we approximately use the half-length of the unit cell in the z -direction for convenience. In the FCP optimization, we add N'_e and F'_e to \mathbf{x}_k and \mathbf{f}_k , respectively.

In eq. (3), \mathbf{h}_k plays a role in determining the step width of not only the new atomic positions but also the new charge N_e . For the Hessian component of N_e , we use the first

derivative of μ with respect to the excess charge ($-\partial\mu/\partial N_e$). In the present implementation, we use the approximate inverse of the density of states (DOS) at μ for $-\partial\mu/\partial N_e$ ($1/\rho(\mu)$). Generally, for a large DOS system near μ_t , μ gradually approaches μ_t because of the small Hessian for N_e evaluated by $1/\rho(\mu)$. Thus, the convergence behavior of the FCP method depends on the DOS near μ_t .

2. GCSCF method

Here, we briefly review the GCSCF method discussed in Ref. 20. The GCSCF reaches constant- μ_e during the SCF loop, is shown as the blue shaded area in Fig. 2. Because the formulation of GCSCF is simple, its calculation flow is essentially the same as that of the conventional DFT with geometry optimization. However, in the GCSCF, N_e is a variable at each SCF step. Generally, we can evaluate N_e by summing the occupied Kohn–Sham (KS) orbitals with the given μ_t . However, such a simple method for evaluating N_e violates the numerical stability of the SCF [15]. Therefore, it is necessary to modify the numerical algorithms to determine the i -th transient Fermi energy (μ^i) and update the electron density during the SCF loop.

Now, we explain the algorithm for determining the μ^i . In the GCSCF, we gradually approach μ^i to μ_t during the SCF as follows: First, we evaluate the Fermi energy ε_F^i at the i -th SCF step by the total number of electrons at the i -th SCF step, using an ordinal method. Second, μ^i is determined by simply mixing ε_F^i and μ_t as follows:

$$\mu^i = \beta\mu_t + (1 - \beta)\varepsilon_F^i, \quad (6)$$

where β is the mixing factor for μ_e ($0 < \beta < 1$). Then, the total number of electrons corresponding to μ^i is determined, and we finally update the occupation number and the electron density using μ^i and the total number of electrons.

Next, we discuss the charge mixing scheme using the direct inversion of the iterative subspace (DIIS) method [35] within the GCSCF framework. At the i -th SCF step, we update the electron density by solving the KS eq. with an input electron density n_{in}^i , and then the updated electron density is used as a n_{in}^{i+1} . However, to obtain a more appropriate value of n_{in}^{i+1} , the updated electron density is mixed with the electron density of the previous SCF steps. To accelerate the convergence of the SCF, we usually use the optimized electron

density obtained by the solution of the DIIS method as n_{in}^{i+1} . Usually, to stabilize the DIIS acceleration, the metric and Kerker preconditioning operators [36] \hat{M} and \hat{K} are introduced, and the DIIS method updates the electron density without altering the term of $n(\mathbf{G} = \mathbf{0})$, where \mathbf{G} is the reciprocal lattice vector. In contrast, the GCSCF requires the total number of electrons to be updated in the SCF loop. Therefore, to update N_e , we introduce the dumping factor of $Q_K (> 0)$ to \hat{K} and \hat{M} as follows:

$$\langle \mathbf{G} | \hat{K} | \mathbf{G} \rangle = \frac{|\mathbf{G}|^2 + Q_K^2}{|\mathbf{G}|^2 + q_K^2 + Q_K^2}, \quad (7)$$

$$\langle \mathbf{G} | \hat{M} | \mathbf{G} \rangle = \frac{4\pi}{|\mathbf{G}|^2 + Q_K^2}. \quad (8)$$

Here, q_K is the original damping factor of the Kerker preconditioning operator. When Q_K is set to zero, \hat{K} and \hat{M} revert to their original values. By introducing Q_K , \hat{K} , and \hat{M} at $\mathbf{G} = \mathbf{0}$ becomes a finite value, and we can always update the total number of electrons in the SCF loop. Once both Ω and μ^i have converged, the ordinal geometry optimization procedure provides the new atomic positions.

3. NEB method combined with constant- μ_e

Here, we briefly discuss the NEB method in combination with the constant- μ_e methods. The NEB method [25–27] describes the minimum energy path (MEP) for a chemical reaction by combining the images of the first and final states. The MEP is determined by solving Eq. (3) until the forces acting on each image become zero. Thus, in the conventional NEB method, we explore the solution of eq. (3) within the space of the $3N \times N_{\text{im}}$ dimension, which corresponds to the motion of N atoms in three dimensions with N_{im} images of the MEP. In the NEB combined with the FCP, eq. (3) is solved within the $(3N + 1) \times N_{\text{im}}$ dimension because we extended the optimization space, as discussed in the previous section. In contrast, when used in combination with the GCSCF, the NEB does not require special modification of the optimization procedure for the conventional NEB framework because of its straightforward formulation. In this work, we employ the Broyden method [37] as a quasi-Newton algorithm for determining the MEPs.

C. Computational details

Here, we provide the computational details of this study. All calculations were performed using the QUANTUM ESPRESSO package [38, 39], which is a DFT code within the plane-wave basis sets and the ultrasoft-pseudopotential [40] framework. We implemented the FCP and GCSCF routines in combination with the ESM method in the package. We used the five-layered slab model in the $p(2 \times 2)$ supercell to represent the Al(111) surface with a single water molecule, which corresponds to a 0.25 monolayer coverage, as shown in Fig. 1(a)]. The two ESM regions with $\epsilon = 1$ and $\epsilon = \infty$ are located at a distance of $\sim 8 \text{ \AA}$ from the outermost Al layers.

For convenience, the experimental lattice constant of the face-centered cubic Al bulk ($4.05 \times 4.05 \times 4.05 \text{ \AA}^3$) [41] was used to construct the surface slab. The cut-off energies for the wavefunctions and charge density were 40 Ry and 320 Ry, respectively. The exchange-correlation functional was the spin unpolarized version of Perdew–Wang 91 within the generalized-gradient approximation [42]. \mathbf{k} -point sampling used a $5 \times 5 \times 1$ mesh in the surface Brillouin zone, and the number of electrons occupying the volume was determined by the Gaussian smearing method with a smearing width of 0.01 Ry. We carried out the structural optimization until $\mathbf{F}_\alpha < 5.0 \times 10^{-4} \text{ Ry/Bohr}$ with the bottom of three Al layers fixed at bulk truncated positions. In the FCP calculation, the convergence thresholds for Ω and F_e , respectively, are set to $1.0 \times 10^{-6} \text{ Ry}$ and $1.0 \times 10^{-2} \text{ eV}$. In the GCSCF calculation, we decrease the threshold of the convergence criteria for Ω to $1.0 \times 10^{-8} \text{ Ry}$, and used the Thomas–Fermi charge-mixing scheme[43]. The NEB [26, 27] calculation under the constant- μ_e condition, which enables the determination of the MEP between two stable endpoints, was carried out to determine the activation barriers and diffusion paths of H_2O molecules at the surface. The NEB calculation was conducted with ten discrete images for the MEP with a path threshold of 0.03 eV/\AA . The activation barriers and diffusion paths converged well for the number of images and path threshold.

III. RESULTS AND DISCUSSIONS

Here, we discuss the results of water adsorption and diffusion on the Al(111) surface as calculated using the NEB method with constant- μ_e .

A. Adsorption site of water-molecule on Al(111)

First, we briefly discuss the adsorption energy and μ_e at the neutral Al(111) surface with a H₂O molecule for adsorption sites, as shown in Fig 1(b). The calculation shows that the on-top sites are the most stable for H₂O adsorption, and the adsorption energy we obtained for these sites is 0.23 eV. These results are consistent with the previous DFT result [12]. For the MEP, we considered H₂O diffusion from one stable on-top site to the next on-top site via a bridge site [44]. To apply the bias voltage U , we measure μ_t from μ_e at the potential of zero charges (PZC), which was -2.91eV . In this study, U is defined as $U = (\mu_t - \mu_{\text{PZC}})/e$ [45], and the three values of U are examined: $U = 0\text{V}$, -1V , and $+1\text{V}$, respectively. Here, μ_{PZC} is μ_e at the PZC.

For comparison purposes, we also carried out the constant- N_e calculations by evaluating the excess charges (ΔN_e) induced by the bias voltage. The results we obtained for ΔN_e under $U = -1\text{V}$ and $U = +1\text{V}$ are $+0.033e$ and $-0.036e$, respectively. The difference in the absolute values of ΔN_e between $U = 1\text{V}$ and -1V implies that the response of surface electrons to the applied bias potential deviates from the linear response regime. In the constant- N_e calculation, we imposed the obtained ΔN_e during the diffusion processes.

B. Activation barrier of water-diffusion on Al(111)

Table I presents the results of the activation barriers E_a obtained by the NEB with the constant- μ_e and $-N_e$ schemes. First, we briefly compare the E_a obtained by the FCP and GCSCF methods (E_a^{FCP} and E_a^{GCSCF}). The results of E_a^{FCP} are almost the same as those of E_a^{GCSCF} . Because the FCP and GCSCF methods converge to the same physical state, this agreement between the methods is reasonable. Hereafter, unless otherwise specified, we discuss the results of E_a using those derived with FCP as being representative of the constant- μ_e scheme.

The result of E_a for the constant- N_e with $\Delta N_e = 0.000e$ is very close to that of the previous climbing image NEB[12]. In contrast, constant- μ_e with $U = 0.0\text{V}$ produces a much lower E_a compared to E_a by the constant- N_e with $\Delta N_e = 0.000e$. Under $U = -1.0\text{V}$, E_a increases to 0.161eV , which is also smaller than the counterpart value of 0.184 eV obtained with the constant- N_e scheme with $N_e = +0.033e$. By switching the value of U from 0.0V to

TABLE I: The activation energies E_a (in eV) of H₂O diffusion on the Al(111) under bias voltages of $U = 0.0V, -1.0V,$ and $+1.0V$ using the constant- μ_e scheme. The results of E_a for the constant- N_e scheme with excess charges ΔN_e are also listed. The superscripts of E_a by the constant- μ_e scheme, respectively, denote the results obtained by the FCP and GCSCF methods.

U	constant- μ_e		constant- N_e	
	E_a^{FCP}	E_a^{GCSCF}	ΔN_e	E_a
0.0 V	0.092	0.091	0.000e	0.143
-1.0 V	0.161	0.161	+0.033e	0.184
+1.0 V	0.024	0.028	-0.036e	0.095

+1.0V, E_a decreases from 0.092eV to 0.024eV. E_a with $U = +1.0V$ is still lower than that determined by using the constant- N_e method with $\Delta N_e = -0.036e$. The above comparison between the constant- μ_e and $-N_e$ methods shows that although they yield similar trends for E_a either as a result of applying bias voltages or introducing excess charges, the results are quantitatively quite different. Compared to the previous experimental data of H₂O-diffusion [8], our results of E_a by the constant- μ_e are in good agreement with the observation that the E_a of water diffusion changes significantly with respect to the bias voltage. Thus, the simulation with the constant- μ_e method plays an important role in reproducing the experimental conditions for a constant bias-potential.

C. MEPs for water-diffusion on Al(111)

Here, we discuss the results of the water diffusion path obtained by the NEB with the constant- μ_e and $-N_e$ schemes. Figure 3 (a)–(c), respectively, show consecutive images of the water diffusion along the MEPs at applied bias voltage of $U = 0V, +1.0V,$ and $-1.0V,$ where we show the results obtained by the FCP as a representative example. Among the ten MEP images of H₂O, we regard the first and last images as identical, and the water molecules are bonded to the surface Al atom via the O atom. Along the diffusion path, the applied bias voltage drastically alters the dipole direction of the water molecule. We can evaluate the change in the direction of the H₂O dipole by obtaining the tilt angle between the dipole normal and the surface (θ). For the first H₂O image, the values of θ under $U = 0.0V,$

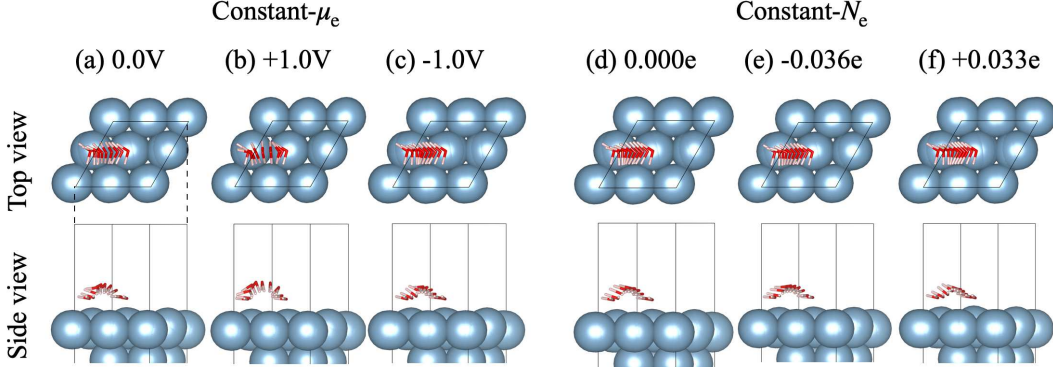


FIG. 3: (Color online). Consecutive views of the MEP (ten images) for water diffusion on Al(111): results of constant- μ_e scheme with bias-voltages of (a) 0.0V, (b) +1.0V, (c) -1.0V, and constant- N_e scheme with the excess charge of (d) 0.000e, (e) $-0.036e$, and (f) $+0.033e$. The cyan, pink, and red spheres represent Al, H, and O atoms, respectively. The upper and lower panels show top and side views of the calculation cell, respectively.

+1.0V, and $-1.0V$ are 76° , 85° , and 71° , respectively. This result indicates that the changes in the adsorption structure of H_2O resulting from the bias voltage are small for the first images of MEPs. However, the value of θ changes drastically in the intermediate images as a consequence of changes in the bias voltage. The dipole direction near the bridge site at $U = 0.0V$ and $+1.0V$ becomes nearly perpendicular to the Al surface, and the H atoms orientate themselves downward. In contrast, the dipole directions for all images tend to be parallel to the surface at $U = -1.0V$.

Figure 3(d)–(f) shows the results obtained for the MEP with the constant- N_e scheme. Here, the first and last images of H_2O in (d), (e), and (f) are the same as those in (a), (b), and (c), respectively. However, the changes in θ in the intermediate images are much smaller than those in the constant- μ_e . Thus, we interpret the difference in the results of E_a between the constant- μ_e and $-N_e$, as presented in Table I, as the difference in the MEPs. Therefore, this dependence of the H_2O geometry along the MEP on the applied bias voltage indicates the importance of the interaction between the water dipole and external electric fields.

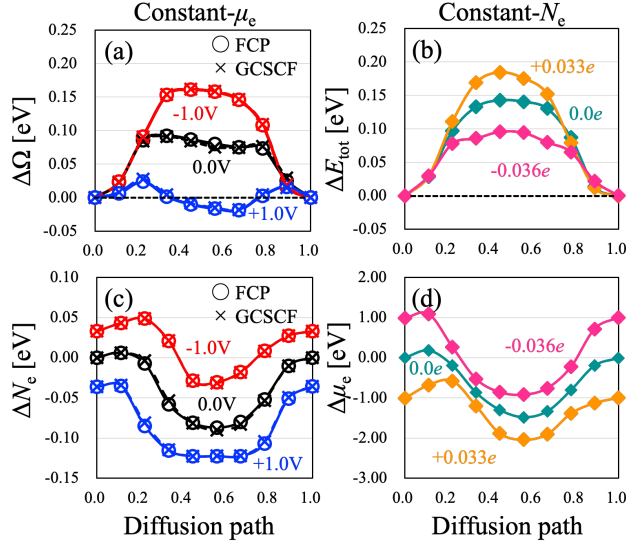


FIG. 4: (Color online). Changes in the (a) grand-potential $\Delta\Omega$, (b) total energies ΔE_{tot} , (c) introduced excess electrons ΔN_e , and (d) chemical potential $\Delta\mu_e$ as a function of the H_2O diffusion path. The results of (a) and (c) are obtained under $U = 0.0\text{V}$, -1.0V , and $+1.0\text{V}$, and the results of (a) and (d) are obtained with $N_e = 0.000e$, $+0.033e$, and $-0.036e$. The open circles and cross symbols denote the results obtained by the FCP and GCSCF methods, respectively. The results of constant- N_e are represented by diamond symbols. The solid and dashed lines are intended to guide the eyes.

D. Details of H_2O diffusion along the MEPs

Figure 4 shows the results of the analysis with NEB. Before discussing the details of the diffusion properties, we briefly discuss the results between the FCP and GCSCF methods shown in Fig. 4(a) and (c). Overall, the results of changes in the grand-potential $\Delta\Omega$ and excess charge ΔN_e along the MEPs obtained by the FCP (represented by open circles) and GCSCF (represented by cross symbols) are the same within the computational accuracy. These results indicate that we successfully implemented the constant- μ_e methods. The main difference between the FCP and GCSCF methods is the computational procedure discussed in Sec. II. Because, as discussed above, we used the extended Hessian in the FCP method, the convergence behavior depends on the inverse of the DOS near μ_t . In contrast, the GCSCF method directly optimizes μ_e during a single SCF calculation. Because these constant- μ_e

methods employ different optimization procedures, we need to consider a different strategy to develop the FCP and GCSCF methods to more efficiently reach the constant- μ_e condition.

Figure 4(a) presents the results of the $\Delta\Omega$, where the black, red, and blue circles, respectively, denote the values under $U = 0.0\text{V}$, -1.0V , and $+1.0\text{V}$. In terms of the overall trend, the heights of $\Delta\Omega$ reach their respective maximum values in the intermediate images and decrease with increasing bias voltage. This behavior indicates that E_a of the diffusion of water on Al(111) depends on the external electric field, as listed in Table I. For $U = +1.0\text{V}$, we found negative values of $\Delta\Omega$ at intermediate images of the diffusion path. This result indicates that the stable adsorption sites of the H_2O molecules on Al(111) change from the on-top sites to sites in the vicinity of the bridge sites. In contrast, the results of ΔE_{tot} shown in Fig. 4(b) obtained by the constant- N_e scheme do not alter the sign of ΔE_{tot} for any values of N_e . Therefore, a comparison of the results of the constant- μ_e and $-N_e$ schemes would necessitate careful adjustment of the bias voltage to determine the stable adsorption site of H_2O on Al(111) in the STM experiments and at the electrochemical interface.

Figure 4(c) shows the results of ΔN_e along the diffusion pathway. In the first images, the values of ΔN_e are the same as those used in the constant- N_e calculations. In the next few images, the value of ΔN_e increases, and then it decreases in the intermediate images of the MEPs. This result is the consequence of introducing excess charges from an external potentiostat to Al(111) to maintain a constant bias voltage. The results obtained for $\Delta\mu_e$ by using the constant- N_e scheme highly depend on the MEPs shown in Fig. 4(d). Here, we define $\Delta\mu_e$ as the difference between the μ_e s in the MEPs and that in the first image of the MEPs of the PZC. Because the total number of electrons is fixed, this result originates from the charge transfer between the H_2O adsorbate and the Al electrode. This charge transfer alters the height of the dipole barrier for the substrate along with the MEPs. Because the change in the surface dipole barrier alters the work function that is directly related to the electrode potential, $\Delta\mu_e$ highly depends on the H_2O diffusion path. Thus, these differences in the control mechanism of the surface charge between the constant- μ_e and $-N_e$ schemes provide the different MEPs for H_2O diffusion at Al(111), as shown in Fig. 3.

IV. SUMMARY

In summary, we demonstrated the realistic simulation of the bias-dependent diffusion of H₂O on the Al(111) surface using NEB calculations within the constant- μ_e scheme. Our results showed that significant differences exist in the activation barrier energies and MEPs, and that this depends on whether the applied bias voltage is positive or negative. A comparison of the constant- μ_e and $-N_e$ schemes also showed that the conventional constant- N_e scheme does not provide a good description of molecular diffusion under a bias voltage owing to the absence of strong interaction between the molecular dipole and the electric field. In comparison, the FCP and GCSCF methods produced the same results within the computational accuracy. We expect the proposed scheme to find a wide variety of applications in the simulation of STM experiments and electrochemical reactions under constant electrode potentials.

Acknowledgments

C.H. and M.O. thank Prof. Osamu Sugino for valuable discussions. This work was supported by MEXT as the “Program for Promoting Research on the Supercomputer Fugaku” (Fugaku Battery & Fuel Cell Project), Grant Number JPMXP1020200301. The computations were performed using the supercomputers of Research Center for Computational Science (Okazaki, Japan), and Institute for Solid State Physics and Information Technology Center at the University of Tokyo.

-
- [1] M. A. Henderson, Surf. Sci. Rep. **46**, 1 (2002).
 - [2] A. Michaelides, V. Ranea, P. De Andres, and D. King, Phys. Rev. Lett. **90**, 216102 (2003).
 - [3] S. Meng, E. Wang, and S. Gao, Phys. Rev. B **69**, 195404 (2004).
 - [4] S. Schnur and A. Groß, New J. Phys. **11**, 125003 (2009).
 - [5] J. Carrasco, A. Hodgson, and A. Michaelides, Nat. Mater. **11**, 667 (2012).
 - [6] H. Ogasawara, B. Brena, D. Nordlund, M. Nyberg, A. Pelenschikov, L. Pettersson, and A. Nilsson, Phys. Rev. Lett. **89**, 276102 (2002).
 - [7] T. Utsunomiya, Y. Yokota, T. Enoki, and K.-i. Fukui, Chem. Commun. **50**, 15537 (2014).

- [8] K. Motobayashi, L. Árnadóttir, C. Matsumoto, E. M. Stuve, H. Jónsson, Y. Kim, and M. Kawai, *ACS Nano* **8**, 11583 (2014).
- [9] P. Hohenberg and W. Kohn, *Phys. Rev.* **136**, B864 (1964).
- [10] W. Kohn and L. J. Sham, *Phys. Rev.* **140**, A1133 (1965).
- [11] V. A. Ranea, A. Michaelides, R. Ramírez, P. L. de Andres, J. A. Vergés, and D. A. King, *Phys. Rev. Lett.* **92**, 136104 (2004).
- [12] V. A. Ranea, *J. Chem. Phys.* **137**, 204702 (2012).
- [13] S. Karkare, L. Boulet, A. Singh, R. Hennig, and I. Bazarov, *Phys. Rev. B* **91**, 035408 (2015).
- [14] T. B. Rawal, S. Hong, A. Pulkkinen, M. Alatalo, and T. S. Rahman, *Phys. Rev. B* **92**, 035444 (2015).
- [15] A. Lozovoi, A. Alavi, J. Kohanoff, and R. Lynden-Bell, *J. Chem. Phys.* **115**, 1661 (2001).
- [16] I. Tavernelli, R. Vuilleumier, and M. Sprik, *Phys. Rev. Lett.* **88**, 213002 (2002).
- [17] W. B. Schneider and A. A. Auer, *Beilstein J. Nanotech.* **5**, 668 (2014).
- [18] U. Benedikt, W. B. Schneider, and A. A. Auer, *Phys. Chem. Chem. Phys.* **15**, 2712 (2013).
- [19] N. Bonnet, T. Morishita, O. Sugino, and M. Otani, *Phys. Rev. Lett.* **109**, 266101 (2012).
- [20] R. Sundararaman, W. A. Goddard III, and T. A. Arias, *J. Chem. Phys.* **146**, 114104 (2017).
- [21] T. Ikeshoji and M. Otani, *Phys. Chem. Chem. Phys.* **19**, 4447 (2017).
- [22] R. Sundararaman, K. Letchworth-Weaver, and K. A. Schwarz, *The Journal of chemical physics* **148**, 144105 (2018).
- [23] J. Haruyama, T. Ikeshoji, and M. Otani, *J. Phys. Chem. C* **122**, 9804 (2018).
- [24] S. E. Weitzner, S. A. Akhade, J. B. Varley, B. C. Wood, E. B. Duoss, S. E. Baker, and M. Otani, *J. Phys. Chem. Lett.* (2020).
- [25] G. Mills, H. Jónsson, and G. K. Schenter, *Surface Science* **324**, 305 (1995).
- [26] G. Henkelman, B. P. Uberuaga, and H. Jónsson, *J. Chem. Phys.* **113**, 9901 (2000).
- [27] G. Henkelman and H. Jónsson, *J. Chem. Phys.* **113**, 9978 (2000).
- [28] A. Michaelides, V. Ranea, P. De Andres, and D. King, *Phys. Rev. B* **69**, 075409 (2004).
- [29] J. Li, Y. Li, S. Zhu, and F. Wang, *Phys. Rev. B* **74**, 153415 (2006).
- [30] M. Otani and O. Sugino, *Phys. Rev. B* **73**, 115407 (2006).
- [31] C. G. Broyden, *J. Inst. Appl. Math.* **6**, 222 (1970).
- [32] R. Fletcher, *Comput. J.* **13**, 317 (1970).
- [33] D. Goldfarb, *Math. Comput.* **24**, 23 (1970).

- [34] D. F. Shanno, *Math. Comput.* **24**, 647 (1970).
- [35] P. Pulay, *J. Comput. Chem.* **3**, 556 (1982).
- [36] G. P. Kerker, *Phys. Rev. B* **23**, 3082 (1981).
- [37] C. G. Broyden, *Math. Comput.* **19**, 577 (1965).
- [38] P. Giannozzi, S. Baroni, N. Bonini, M. Calandra, R. Car, C. Cavazzoni, D. Ceresoli, G. L. Chiarotti, M. Cococcioni, I. Dabo, et al., *J. Phys.: Condens. Matter* **21**, 395502 (2009).
- [39] P. Giannozzi, O. Andreussi, T. Brumme, O. Bunau, M. B. Nardelli, M. Calandra, R. Car, C. Cavazzoni, D. Ceresoli, M. Cococcioni, et al., *J. Phys.: Condens. Matter* **29**, 465901 (2017).
- [40] D. Vanderbilt, *Phys. Rev. B* **41**, 7892 (1990).
- [41] S. Popović, B. Gržeta, V. Ilakovac, R. Kroggel, G. Wendrock, and H. Löffler, *Phys. Status Solidi A* **130**, 273 (1992).
- [42] J. P. Perdew, J. A. Chevary, S. H. Vosko, K. A. Jackson, M. R. Pederson, D. J. Singh, and C. Fiolhais, *Phys. Rev. B* **46**, 6671 (1992).
- [43] D. Raczkowski, A. Canning, and L. W. Wang, *Phys. Rev. B* **64**, 121101 (2001).
- [44] The first and the last images of the NEB calculation were prepared by the most stable adsorption structure at a bias U . Then the intermediate images were initialized using the interpolation scheme both for the geometry and charge.
- [45] The sign of U is set as in the STM: A positive sample bias drives the electron injected into the sample and increases the Fermi energy with respect to the μ_{pzc} .